The Astrophysical Journal, 759:15 (8pp), 2012 November 1 doi:10.1088/0004-637X/759/1/15

MULTI-WAVELENGTH SPECTROSCOPIC OBSERVATION OF EXTREME-ULTRAVIOLET JET IN AR 10960

Y. Matsui[1], T. Yokoyama[1], N. Kitagawa[1], and S. Imada[2]
[1] Department of Earth and Planetary Science, University of Tokyo, 7-3-1 Hongo, Bunkyo-ku, Tokyo 113-0033, Japan
[2] Solar-Terrestrial Environment Laboratory, Nagoya University, Furo-cho, Chikusa-ku, Nagoya 464-8601, Japan
Received 2012 May 2; accepted 2012 September 4; published 2012 October 11

ABSTRACT

We have studied the relationship between the velocity and temperature of a solar EUV jet. The highly accelerated jet occurred in the active region NOAA 10960 on 2007 June 5. Multi-wavelength spectral observations with EIS/*Hinode* allow us to investigate Doppler velocities at a wide temperature range. We analyzed the three-dimensional angle of the jet from stereoscopic analysis with *STEREO*. Using this angle and Doppler velocity, we derived the true velocity of the jet. As a result, we found that the cool jet observed with He II 256 Å $\log_{10} T_e[\mathrm{K}] = 4.9$ is accelerated to around 220 km s^{-1}, which is over the upper limit of the chromospheric evaporation. The velocities observed with the other lines are below the upper limit of the chromospheric evaporation, while most of the velocities of the hot lines are higher than those of cool lines. We interpret that the chromospheric evaporation and magnetic acceleration occur simultaneously. A morphological interpretation of this event based on the reconnection model is given by utilizing the multi-instrumental observations.

Key words: magnetic fields – Sun: corona – Sun: flares

Online-only material: color figures

1. INTRODUCTION

Solar jets are known as the plasma ejection in the solar corona and strongly believed to be produced by magnetic reconnection. X-ray jets were first observed (Shibata et al. 1992; Strong et al. 1992) with the soft X-ray telescope (SXT; Tsuneta et al. 1991) on board *Yohkoh* (Ogawara et al. 1991). Alexander & Fletcher (1999) observed the solar jets in the extreme ultraviolet (EUV) with the *Transition Region and Coronal Explorer* (*TRACE*; Handy et al. 1999), and revealed those detailed structures. The statistical studies of X-ray jets were presented by Shimojo et al. (1996) using statistics from SXT/*Yohkoh* and Savcheva et al. (2007) which were obtained by using the X-Ray Telescope (XRT; Golub et al. 2007) on board *Hinode* (Kosugi et al. 2007).

The physical model of jets was established by Shibata et al. (1994). In this model, the trigger of the jet is the magnetic reconnection between the emerged flux and preexisting coronal magnetic field. There are two types of acceleration mechanisms in this model. One is the magnetic acceleration due to magnetic reconnection and the other is the thermal acceleration due to chromospheric evaporation. Since the jet is caused by the magnetic reconnection, at least a part of the jet is accelerated by the magnetic force, and its velocity reaches the Alfvén velocity. Two-dimensional MHD simulations performed by Yokoyama & Shibata (1995, 1996) successfully reproduced the magnetic acceleration by the magnetic reconnection. The blowout jet (Moore et al. 2010) is a type of magnetic acceleration mechanism. In this model, the magnetic reconnection causes blowout eruption of the cool filament. In the reconnection model, the chromospheric evaporation (i.e., acceleration by the high pressure caused through the thermal energy input from the magnetic reconnection site or non-thermal particles) occurs simultaneously. Shimojo et al. (2001) performed one-dimensional hydrodynamic simulations and succeeded in reproducing the evaporation flow. Miyagoshi & Yokoyama (2004) succeeded in reproducing the evaporation flow caused by magnetic reconnection in MHD simulations. The velocity by the thermal acceleration depends on the temperature. This temperature dependence was observed in the chromospheric evaporation by the flare (Milligan & Dennis 2009) and dimming flows (Imada et al. 2007, 2011). A theoretical upper limit of the chromospheric evaporation velocity is approximately $2.35\,C_s$, where C_s is the sound speed (Fisher et al. 1984).

In order to analyze the acceleration of the jet, the spectroscopic observation is effective because the temperature and velocity of the plasma are obtained from the spectroscopic observation. However, previous spectroscopic observations (Culhane et al. 2007b; Kamio et al. 2010) did not reveal the mechanism of the acceleration of the jet. Our objective in this study is to establish the detailed acceleration mechanism of the solar jets with the multi-wavelength spectroscopic observation. In this paper, we study simultaneous observations by multiple instruments of a jet on 2007 June 5. We mainly use the data of the EUV imaging spectrometer (EIS; Culhane et al. 2007a) on board *Hinode* which is very useful in understanding the plasma dynamics of the jet. We also use the XRT on board *Hinode*, *TRACE* 171 Å and 1600 Å data to study the detailed morphology and temporal variation, the Sun Earth Connection Coronal and Heliospheric Investigation (SECCHI; Howard et al. 2008)/EUV Imager (EUVI; Wuelser et al. 2004) on board the *Solar Terrestrial Relations Observatory* (*STEREO*: Kaiser et al. 2008) to study the inclination angle of the jet, the Michelson Doppler Imager (MDI; Scherrer et al. 1995) on board the *Solar and Heliospheric Observatory* (*SOHO*; Domingo et al. 1995) to obtain the magnetic field, and the Solar Magnetic Activity Research Telescope (SMART; UeNo et al. 2004) at Hida Observatory to investigate the response of the chromosphere.

2. DATA SET

EIS has high spectral and spatial resolution and obtains the imaging and spectral data simultaneously by raster scan. On 2007 June 5 04:16 UT, EIS started the raster scan on the active region NOAA 10960 which consisted of 120 slit positions with slit width of 2″ and height 240″ and with field of view of 240″ × 240″. Each exposure was 5 s, the cadence

was 6 s, and the total duration was 12 minutes. The data in 17 spectral windows are obtained for this data set. We calibrate the EIS data using the standard processing routine eis_prep in SolarSoftWare, which removes the dark current, cosmic-ray affected data, and hot pixels. The slit tilt and the orbital variation of the line position are corrected using the eis_tilt_correction routine and the eis_orbit_spline routine, respectively.

We also use XRT. All XRT data in this study were taken with the Ti_poly filter. The maximum of the temperature response of this filter is close to 8 MK (Kano et al. 2004), and this temperature is higher than all of the emission lines which we analyze in this paper. XRT data are calibrated by using xrt_prep in SolarSoftWare and normalized with each exposure time. XRT was observed at the unequal cadence and there were time when XRT was not observed. *TRACE* has the capability to take EUV images with a high spatial resolution of 1″. Thus, its data are useful in studying the detail of the EUV jet's structures and temporal variation. When EIS observed NOAA 10960, *TRACE* also observed this active region in Fe IX/Fe X 171 Å with a cadence of 60 s. The *TRACE* field of view is 8.′5 × 8.′5, and the EIS field of view is covered by *TRACE* in this observation. *TRACE* also observed this active region with 1600 Å with a cadence of almost one hour. We use one 1600 Å image at 04:31 UT. *TRACE* data are corrected by standard processing routine trace_prep, which removes the dark current, cosmic rays, and a readout pedestal.

EUVI data from both *STEREO-A* and *STEREO-B* are also available. We use EUVI to calculate an inclination angle of the jet. The separation angle in terms of the sun between *STEREO-A* and *STEREO-B* was 11° when *STEREO-A* and *STEREO-B* observed the jet, which is suitable for calculating the inclination angle of the jet. The Solar Optical Telescope on board *Hinode* (SOT; Tsuneta et al. 2008) did not observe this active region, so we cannot obtain the detailed structure of the magnetic field. Instead, MDI full-disk magnetograms are obtained. The cadence was 96 minutes, and we use the data at 03:15 UT. The Hα images of this active region are available from SMART-T3 around 2007 June 5 04:16 UT.

All images are co-aligned with each other. The co-alignment of the images from different instruments is done based on structures seen at similar temperatures. First we compare the MDI magnetogram with the *TRACE* 1600 Å image and co-align them with the position of the sunspot. *TRACE* 171 Å and 1600 Å images are co-aligned at 04:31 UT, then other 171 Å images are de-rotated to a reference time of 04:31 UT. EIS 195 Å images are compared with *TRACE* 171 Å images at 04:18 UT. The relative positional offset in the data sets of EIS obtained by its two CCDs (in bands 246–292 Å and 170–211 Å) is corrected by using the procedure eis_ccd_offset in SolarSoftWare. XRT images are co-aligned with *TRACE* 171 Å images. Finally, we compare the SMART-T3 Hα image with the MDI magnetogram and co-aligned them using the position of the sunspot.

3. RESULTS

3.1. Three-dimensional Structure of the Jet

The jet occurred in the active region NOAA 10960 (S03, E25) around 04:18 UT, 2007 June 5. Figure 1 shows the images observed with *TRACE*, XRT, and EIS. Figures 1(a)–(e) show EUV images observed with *TRACE* 171 Å. An EUV jet J1 is shown in Figure 1(b). After J1 was observed, a second EUV jet J2 was observed (Figure 1(d)). Figures 1(f), (h), (i), and (j) show the X-ray images observed with the XRT Ti_poly filter. Figure 1(f)

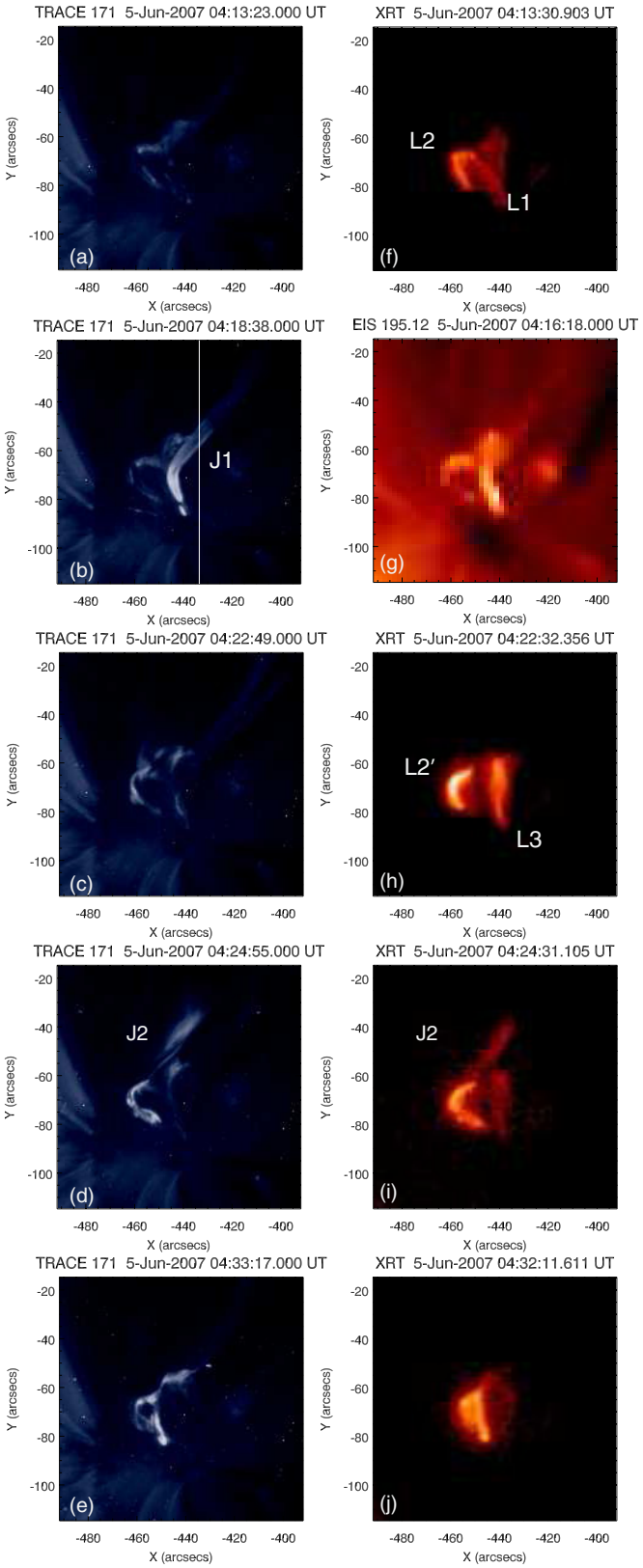

Figure 1. (a)–(e) EUV images observed with *TRACE* 171 Å. The vertical white line in (b) corresponds to the position of the EIS slit at the *TRACE* observation time. (f), (h), (i), and (j) X-ray images observed with XRT with the Ti_poly filter. (g) the EIS intensity image in Fe XII 195 Å.

(A color version of this figure is available in the online journal.)

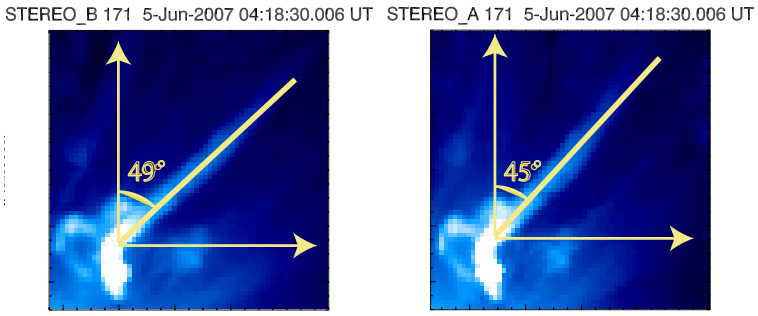

Figure 2. Left panel shows J1 observed from *STEREO-B*, and the right panel shows J1 observed with *STEREO-A*. Yellow lines represent the observed inclination angle of J1 in each plane.

(A color version of this figure is available in the online journal.)

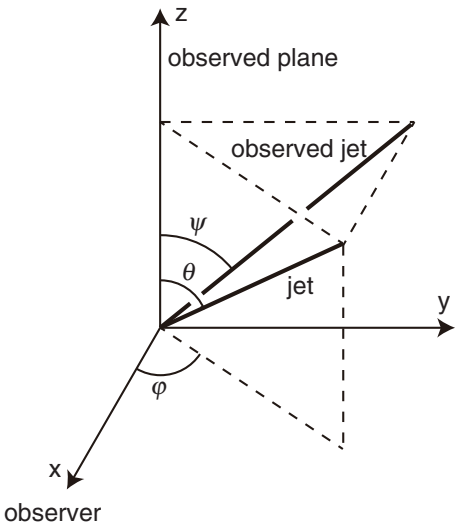

Figure 3. Polar coordinate system view of the jet. The x-axis is toward the observer, and z-axis is parallel to the direction of the solar north pole. The origin of this system is the footpoint of the jet.

shows bright loops L1′ and L2′ which appear before J1. The X-ray image of J1 is unavailable due to the data gap of the XRT observation. After J2, there are new loops (Figure 1(h)). After J1 occurred, L2 changes into L2′ and L3 appears. Figure 1(i) shows J2 in X-ray at the same time of Figure 1. EIS observed J1 with a raster scan. Figure 1(g) shows the EIS intensity map in Fe XII 195 Å. In this paper, we analyze the multi-wavelength spectroscopic observation of J1.

The three-dimensional structure can be obtained from the *STEREO-A* and *STEREO-B* images taken from the different viewing angles. The right (left) panel of Figure 2 shows J1 observed with *STEREO-A* (*STEREO-B*). Figure 3 is a polar coordinate system view of the jet. In this coordinate system, the x-axis is toward the observer and the z-axis is parallel to the direction of the solar north pole. The origin of this system is the footpoint of the jet. The direction of the x-axis depends on the position of the observer as in the case of *STEREO-A* and *STEREO-B*. The origin and z-axis do not change for any observers. The inclination and azimuth of the jet are θ and ϕ, respectively. The observed jet in Figure 3 is the projection on the yz-plane. The apparent inclination of the observed jet is ψ in this figure. This angle is expressed using θ and ϕ,

$$\tan\psi = \tan\theta \sin\phi. \quad (1)$$

From the position of *STEREO-A* and *STEREO-B*, the azimuths are $\phi_A = \phi_E - \alpha$ and $\phi_B = \phi_E + \beta$, respectively, where ϕ_E is the azimuth for observers at the Earth. α (β) is the angle between *STEREO-A* (*STEREO-B*) and the Earth around the sun. The inclination θ is independent of the position of the considering observers. The apparent inclinations observed with *STEREO-A* and *STEREO-B* are $\psi_A = 45°$ and $\psi_B = 49°$, respectively, and are overplotted in Figure 2. ψ_A and ψ_B are described using Equation (1),

$$\frac{\tan\psi_A}{\tan\psi_B} = \frac{\sin(\phi_E - \alpha)}{\sin(\phi_E + \beta)}. \quad (2)$$

When *STEREO-A* and *STEREO-B* observed the jet, their locations are at $\alpha = 7.^\circ24$ and $\beta = 4.^\circ07$. The azimuth and inclination are derived from Equation (2) and $\phi_E = 56.^\circ3$ and $\theta = 52.^\circ9$, respectively.

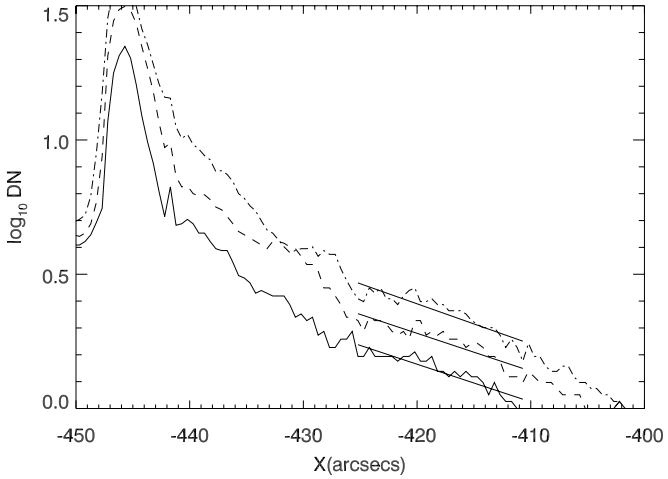

Figure 4. Intensity distributions along J1 observed with *TRACE* 171 Å at 04:16 UT shown by the solid line, 04:17 UT by the dashed line, and 04:18 UT by the dash-dotted line.

3.2. Velocity

Figure 4 is the intensity distribution along J1 observed with *TRACE* 171 Å at 04:16 UT in solid line, 04:17 UT in dashed line, and 04:18 UT in dash-dotted line. The distributions of the intensity in each exposure time are well described by an exponential function, that is consistent with Shimojo et al. (1996, 2001). The temporal offsets of the intensity profile have a speed of 155 km s^{-1}. We interpret this as a projection velocity of the plasma motion along J1 at the temperature of this filter range.

EIS observed J1 with many emission lines. The observed emission lines and their formation temperatures are summarized in Table 1. Figure 5 shows the intensity images observed

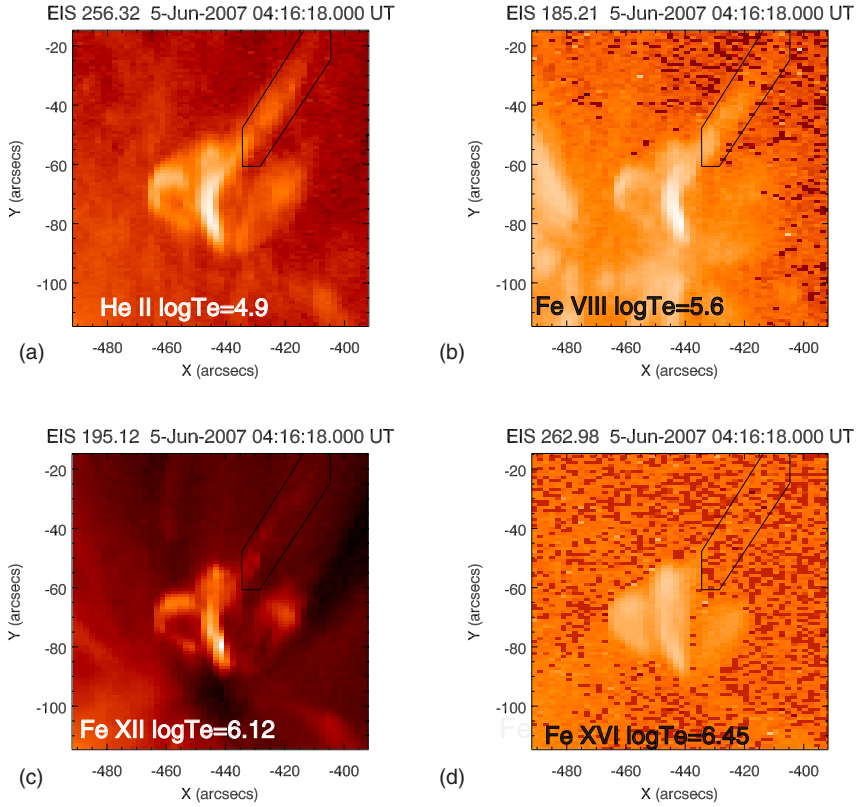

Figure 5. EIS intensity images of J1 observed with (a) He II, (b) Fe VIII, (c) Fe XII, and (d) Fe XVI, respectively. The FOV of the figures is part of the EIS raster scan and corresponds to the *TRACE* and XRT images in Figure 1.

(A color version of this figure is available in the online journal.)

Table 1
The Observed Emission Lines and their Formation Temperatures

Ion	Wavelength λ (Å)	$\log_{10} T_e$ [K]
He II	256.32	4.90
Fe VIII	185.21	5.60
Si VII	275.35	5.80
Fe X	184.54	6.05
Fe XII	186.88	6.12
Fe XII	195.12	6.12
Fe XIII	202.04	6.25
Fe XIII	203.83	6.25
Fe XIV	274.20	6.30
Fe XIV	264.78	6.30
Fe XV	284.16	6.35
Fe XVI	262.98	6.45

with (a) He II 256 Å ($\log_{10} T_e$[K] = 4.9), (b) Fe VIII 185 Å ($\log_{10} T_e$[K] = 5.6), (c) Fe XII 195 Å ($\log_{10} T_e$[K] = 6.12), and (d) Fe XVI 262 Å ($\log_{10} T_e$[K] = 6.45), respectively. The field of view (hereafter FOV) of Figure 5 is part of the EIS raster scan and corresponds to that of the *TRACE* and XRT images in Figure 1. The scan of Figure 5 started at 04:16 UT and ended at 04:21UT. Figures 5(a) and (b) are examples of the cool lines and Figures 5(c) and (d) are examples of the hot lines. The jet is clearly identified in the cool lines while it is not clear in the hot lines. The Doppler velocity images are shown in Figures 6(a)–(d). Doppler velocities are obtained by fitting the spectrum with a single Gaussian function and calculated from the displacement of the center of the fitting Gaussian function using the eis_auto_fit in SolarSoftWare. The blueshift of the jet is clearly shown in Figures 6(a)–(c) but is not clear in Figure 6(d) because of the weak intensity and large noise of Fe XVI 262 Å.

We determine the jet region shown by the black lines in Figures 5 and 6 by a visual inspection. In this region, the intensity of He II is bright. He II, Fe VIII and Fe XII show the strong blueshift in this region. Figure 7 shows the line profiles averaged in the jet region. All lines show strong blueshift even in Fe XVI. The blending effect of the neighboring Si X 256.37 Å ($\log_{10} T_e$[K] = 6.2) with the He II blueshifted component is weak because it can be estimated by using the ratio of the blueshifted component to the rest component of Fe XII. The effect of the hotter Fe XVII 262.8 Å line around the blueshift component of Fe XVI is negligible because the expected intensity from the CHIANTI atomic database (Landi et al. 2006; Dere et al. 1997) and Fe XVII 254.9 Å observed with EIS is much smaller than that of the blueshift component.

The spectrum of each line (summarized in Table 1) is averaged in the jet region and fitted with a double Gaussian function to derive the Doppler velocities of the blueshift component. The true velocity of the jet is derived from the Doppler velocity and projection velocity,

$$V_{\rm jet} = \frac{V_{\rm Doppler}}{\sin\theta\cos\phi_{\rm E}} \quad (3)$$

$$= \frac{V_{\rm projection}}{\sqrt{1-\sin^2\theta\cos^2\phi_{\rm E}}}, \quad (4)$$

where $V_{\rm jet}$, $V_{\rm Doppler}$, and $V_{\rm projection}$ are the jet velocity, Doppler velocity, and projection velocity, respectively. The azimuth $\phi_{\rm E}$ and inclination θ are derived by Equation (2). The relationship

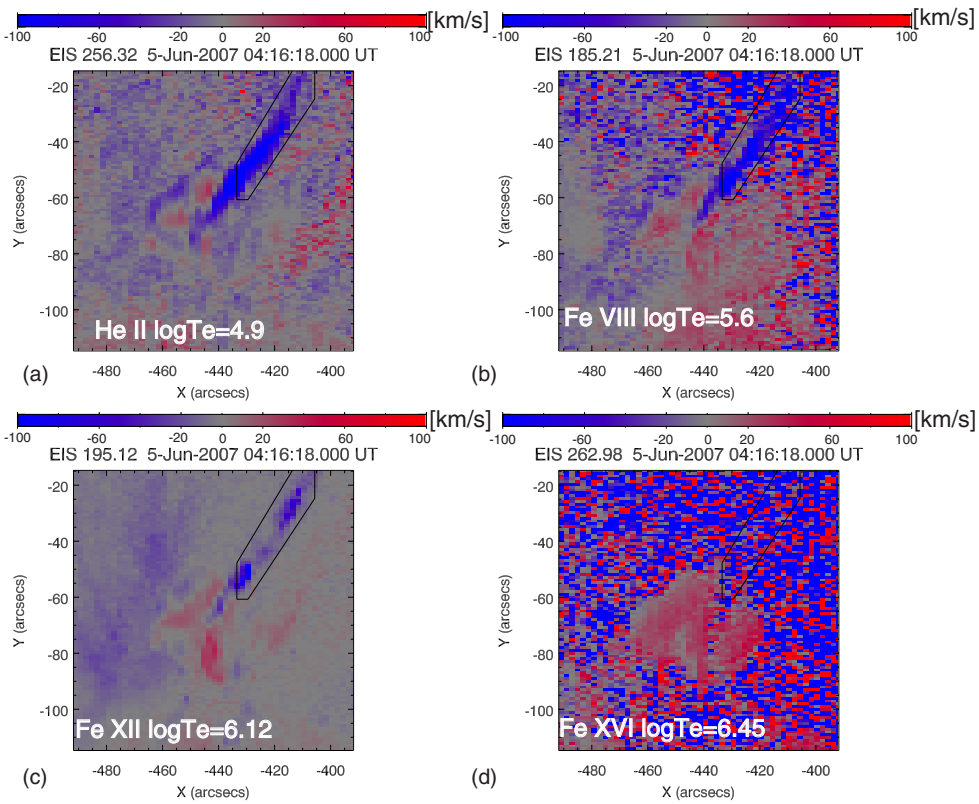

Figure 6. Doppler velocity images corresponding to the data set in Figures 5(a)–(d), respectively.

of the temperature and thus derived true jet velocity is shown in Figure 8. The temperature of the jet is defined by the line formation temperature (Table 1) and its error is estimated by the FWHM of the contribution function based on the CHIANTI atomic database. The error bar of the velocity indicates the error of the double Gaussian fitting. The velocity derived from the projection velocity of *TRACE* 171 Å is indicated by the triangle symbol. The temperature of this component is defined by the temperature response of *TRACE* 171 Å filter (Handy et al. 1999). The FWHM of the temperature response is shown as an error bar on the triangle symbol in Figure 8. The solid line in Figure 8 shows the sound speed and the dashed line shows a theoretical upper limit to the chromospheric evaporation velocities derived in Fisher et al. (1984).

3.3. Magnetic and Chromospheric Features

Figure 9(a) shows the magnetic field observed with *SOHO*/MDI. The red and blue contours represent the positive and negative line-of-sight magnetic fields, respectively, and the background shows the *TRACE* 171 Å intensity at the J1 occurrence time. It is found that J1 occurred near the large negative sunspot and positive polarities (P1 and P2). From the overlaid plot on the X-ray image in Figure 9(b), we find that the eastern (L2′ in Figure 1(h)) and western (L3) loops connect P1 and P2 with the sunspot, respectively. Figures 9(c) and (d) show the Hα and 1600 Å intensities at the J2 occurrence time (see also Figures 1(e) and (j)). In both panels, we see two ribbons, each of which corresponds to each magnetic polarity. One of the ribbons is located at P1's position, suggesting that they are footpoints of loop L2′. We will discuss the geometrical magnetic structure driving the jets in Section 4.1 based on these observations.

4. DISCUSSION

4.1. Geometrical Interpretation of Global Magnetic Structure

We consider the global magnetic field structure (Figure 10) consistent with the observed jets, loops (Figure 1), magnetic fields, and flare ribbons (Figure 9). The red and blue lines are the positive and negative magnetic fields on the photosphere observed with MDI, respectively, and the black lines represent the interpreted magnetic field lines. Before the onset of the jet (Figure 10(a)), an open magnetic field F1 is connected with the sunspot. There are also closed magnetic loops (L1′, L2′) between the positive magnetic field P1 and the sunspot. Another positive magnetic field P2 is also connected with the sunspot by a closed loop (L3). The first jet J1 is produced by the reconnection which occurred between the closed loop L1 and open field F1 in Figure 10(a). This scenario is a kind of a standard jet (Shibata et al. 1994). As a result of the reconnection between these two fields, field lines F1′ and L1′ are produced. F1′ is greatly bent because of L3 in Figure 10(b). F1′and L3 reconnect again and L3 becomes bright in Figure 1(g) around $y = 80''$. L3 seems to be filled with the dense plasma caused by the chromospheric evaporation. L3 also shows redshift in Figure 6(c), which might be the shrinking of the reconnected field lines with plasma. Flare ribbons in Figures 9(c) and (d) around the footpoints of L1′ and L2′ are thought to be due to another reconnection between L1′ and L2. The second jet J2 is considered to be related to another open magnetic field, F2, shown in Figure 10(b) as a dashed line, which is not seen in the observations. Another possibility for J2 is a blowout eruption of the sheared core field around L2 (Moore et al. 2010). In this interpretation, L2″ in Figure 10(b) is the erupted loop. This eruption is triggered by the reconnection

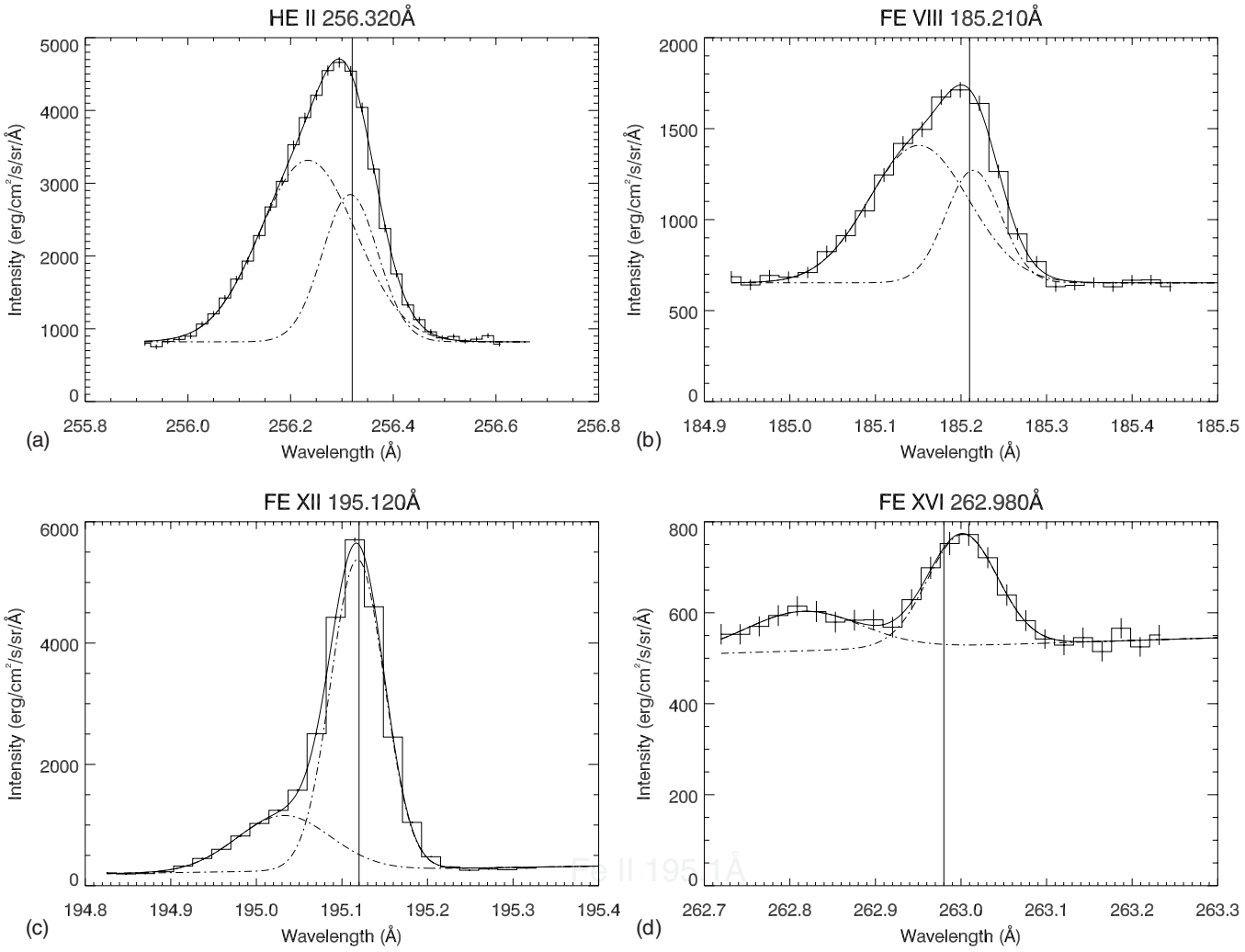

Figure 7. Line profiles averaged in the jet region. Panels (a)–(d) correspond to the data set for Figures 5(a)–(d), respectively. The histogram is the data with photon-noise error bars, the solid line is the fitted profile, and the dash-dotted lines are its components. The vertical solid line indicates the line center of the emission line.

that produced J1. In this case, the first standard jet creates the second blowout jet.

4.2. Magnetic and Thermal Acceleration

EIS observed strong blueshifts in the multiple lines covering the wide temperature range as shown in Figure 8. The profiles in Figure 7 show the blueshifts of the observed lines. At the temperature (Fe XII and Fe XVI), the intensities of the blueshift components are weaker than the rest one. At the low temperature line (He II and Fe VIII), on the other hand, the intensities of the blueshift components are stronger than the rest one. This implies that the density of the cool plasma in the jet is larger than that of background cool plasma, which probably relates to the difference of the acceleration of the cool and hot plasma though the reason therefore is not revealed clearly in this study.

Finally, we discuss the difference of the acceleration of the cool and hot plasma. We consider the two types of acceleration, i.e., magnetic acceleration due to magnetic reconnection and thermal acceleration due to chromospheric evaporation. The thermal accelerations like the chromospheric evaporation (Milligan & Dennis 2009) and dimming flows (Imada et al. 2007, 2011) show a dependence of the velocity on the temperature.

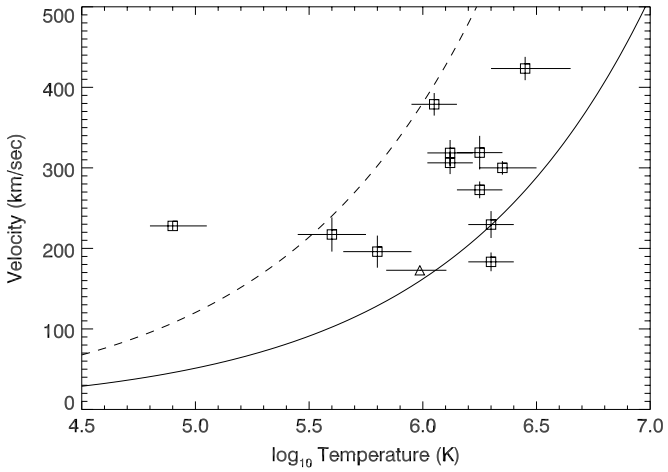

Figure 8. Relationship of the temperature and velocities observed with EIS and *TRACE*. The jet velocities are derived from Doppler shifts observed with EIS (square symbols) and projection velocity observed with *TRACE* (triangle symbol) using Equations (3) and (4). Solid line shows the sound speed and dashed line shows a theoretical upper limit to chromospheric evaporation velocities by Fisher et al. (1984).

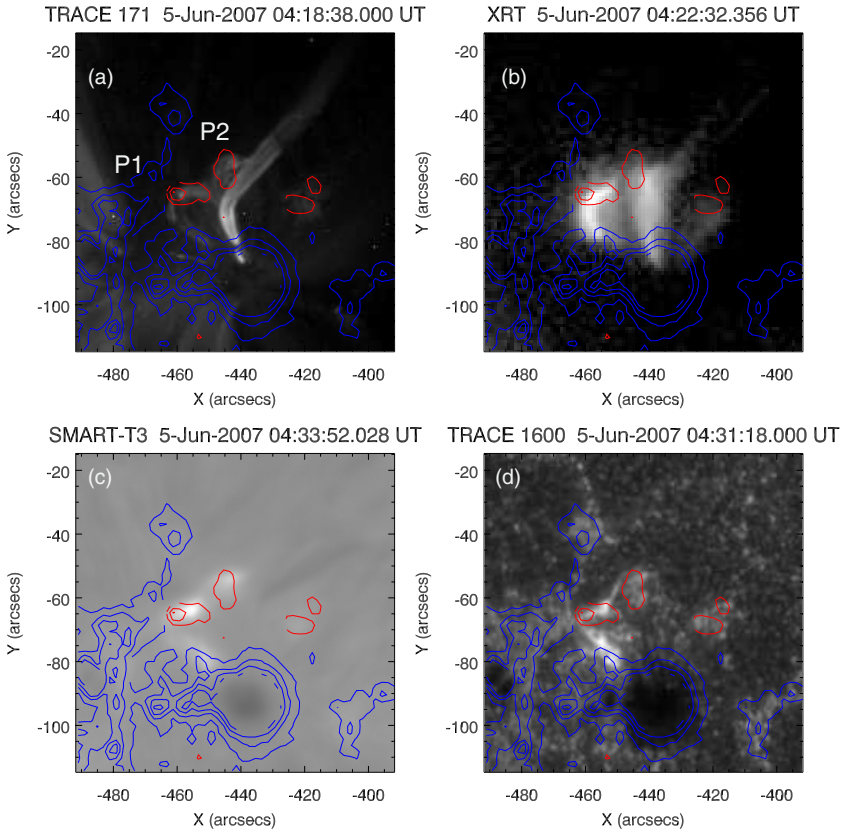

Figure 9. Red and blue contours represent the positive and negative line-of-sight magnetic fields observed with *SOHO*/MDI, respectively. Background images show (a) the *TRACE* 171 Å intensity image at J1 occurrence, (b) the X-ray intensity taken with the Ti_poly filter of XRT, (c) the Hα image taken with SMART-T3, and (d) the *TRACE* 1600 Å image after the J2 occurrence.

(A color version of this figure is available in the online journal.)

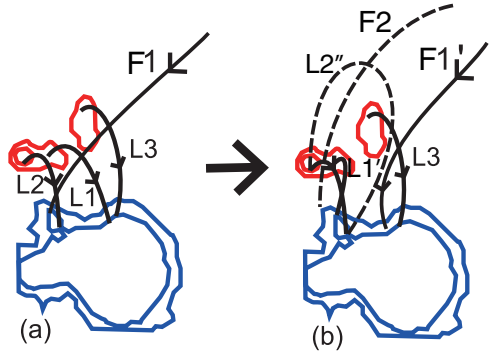

Figure 10. Schematic pictures of our interpretation on the geometrical magnetic structure. The red and blue lines are the positive and negative magnetic fields on the photosphere observed with MDI, respectively, and the black lines represent the magnetic field. The left (right) positive red polarity is P1 (P2). Each panel shows (a) before the onset of J1 and (b) around the time of J1.

(A color version of this figure is available in the online journal.)

If the jet is accelerated by chromospheric evaporation, the velocity of the jet increases with increasing temperature along with the sound speed. Its theoretical upper limit is approximately 2.35 C_s (Fisher et al. 1984). The velocities of the hot plasma described in Figure 8 show a tendency to change along with the sound speed within this upper limit, which is consistent with the chromospheric evaporation. On the other hand, the velocity of He II is much faster than this upper limit. This probably suggests that He II is accelerated by magnetic acceleration. We interpret that the magnetic acceleration also occurs in the jet along with the chromospheric evaporation. In other words, hot plasma is accelerated by chromospheric evaporation while cool plasma is accelerated by magnetic force. This magnetic acceleration of the cool plasma is consistent with a blowout jet (Moore et al. 2010). In this jet, two types of accelerations, i.e., the magnetic and thermal accelerations, occur at the same time. This result is consistent with the magnetic reconnection model.

5. SUMMARY

We analyze the fine structure of a solar EUV jet based on the magnetic reconnection model. Multi-wavelength spectral observations with EIS allow us to know the Doppler velocities at a wide temperature range. We find that this jet is accelerated by thermal acceleration and magnetic acceleration at the same time. Our results are consistent with the magnetic reconnection model. To confirm our conclusion, we will perform a numerical simulation and reproduce the jet under a condition similar to the observation in this paper in future work.

Hinode is a Japanese mission developed and launched by ISAS/JAXA, collaborating with NAOJ as a domestic partner, NASA and STFC (UK) as international partners. Scientific operation of the *Hinode* mission is conducted by the *Hinode* science team organized at ISAS/JAXA. This team mainly consists of scientists from institutes in the partner countries. Support for the post-launch operation is provided by JAXA and NAOJ (Japan), STFC (UK), NASA, ESA, and NSC (Norway). We are deeply grateful for the proofreading/editing assistance from the GCOE program.

REFERENCES

Alexander, D., & Fletcher, L. 1999, Sol. Phys., 190, 167
Culhane, J. L., Harra, L. K., James, A. M., et al. 2007a, Sol. Phys., 243, 19
Culhane, L., Harra, L. K., Baker, D., et al. 2007b, PASJ, 59, 751
Dere, K. P., Landi, E., Mason, H. E., Monsignori Fossi, B. C., & Young, P. R. 1997, A&AS, 125, 149
Domingo, V., Fleck, B., & Poland, A. I. 1995, Sol. Phys., 162, 1
Fisher, G. H., Canfield, R. C., & McClymont, A. N. 1984, ApJ, 281, L79
Golub, L., Deluca, E., Austin, G., et al. 2007, Sol. Phys., 243, 63
Handy, B. N., Acton, L. W., Kankelborg, C. C., et al. 1999, Sol. Phys., 187, 229
Howard, R. A., Moses, J. D., Vourlidas, A., et al. 2008, Space Sci. Rev., 136, 67
Imada, S., Hara, H., Watanabe, T., et al. 2007, PASJ, 59, 793
Imada, S., Hara, H., Watanabe, T., et al. 2011, ApJ, 743, 57
Kaiser, M. L., Kucera, T. A., Davila, J. M., et al. 2008, Space Sci. Rev., 136, 5
Kamio, S., Curdt, W., Teriaca, L., Inhester, B., & Solanki, S. K. 2010, A&A, 510, L1
Kano, R., Hara, H., Shimojo, M., et al. 2004, in ASP Conf. Ser. 325, The Solar-B Mission and the Forefront of Solar Physics, ed. T. Sakurai & T. Sekii (San Francisco, CA: ASP), 15
Kosugi, T., Matsuzaki, K., Sakao, T., et al. 2007, Sol. Phys., 243, 3
Landi, E., Del Zanna, G., Young, P. R., et al. 2006, ApJS, 162, 261
Milligan, R. O., & Dennis, B. R. 2009, ApJ, 699, 968
Miyagoshi, T., & Yokoyama, T. 2004, ApJ, 614, 1042
Moore, R. L., Cirtain, J. W., Sterling, A. C., & Falconer, D. A. 2010, ApJ, 720, 757
Ogawara, Y., Takano, T., Kato, T., et al. 1991, Sol. Phys., 136, 1
Savcheva, A., Cirtain, J., Deluca, E. E., et al. 2007, PASJ, 59, 771
Scherrer, P. H., Bogart, R. S., Bush, R. I., et al. 1995, Sol. Phys., 162, 129
Shibata, K., Ishido, Y., Acton, L. W., et al. 1992, PASJ, 44, L173
Shibata, K., Nitta, N., Matsumoto, R., et al. 1994, in X-Ray Solar Physics from Yohkoh, ed. Y. Uchida, T. Watanabe, K. Shibata, & H. S. Hudson (Tokyo: Universal Academy Press), 29
Shimojo, M., Hashimoto, S., Shibata, K., et al. 1996, PASJ, 48, 123
Shimojo, M., Shibata, K., Yokoyama, T., & Hori, K. 2001, ApJ, 550, 1051
Strong, K. T., Harvey, K., Hirayama, T., et al. 1992, PASJ, 44, L161
Tsuneta, S., Acton, L., Bruner, M., et al. 1991, Sol. Phys., 136, 37
Tsuneta, S., Ichimoto, K., Katsukawa, Y., et al. 2008, Sol. Phys., 249, 167
UeNo, S., Nagata, S., Kitai, R., Kurokawa, H., & Ichimoto, K. 2004, Proc. SPIE, 5492, 958
Wuelser, J., Lemen, J. R., Tarbell, T. D., et al. 2004, Proc. SPIE, 5171, 111
Yokoyama, T., & Shibata, K. 1995, Nature, 375, 42
Yokoyama, T., & Shibata, K. 1996, PASJ, 48, 353